Nano Research
2022, 15(6): 5663–5670

ISSN 1998-0124 CN 11-5974/O4
https://doi.org/10.1007/s12274-022-4123-y

Research Article

Characterization and modeling of the temperature-dependent thermal conductivity in sintered porous silicon-aluminum nanomaterials

Danny Kojda[1] (✉), Tommy Hofmann[1], Natalia Gostkowska-Lekner[1,2], and Klaus Habicht[1,2]

[1] *Department Dynamics and Transport in Quantum Materials, Helmholtz-Zentrum Berlin für Materialien und Energie GmbH, Berlin D-14109, Germany*
[2] *Institute of Physics and Astronomy, University of Potsdam, Potsdam D-14476, Germany*

© The Author(s) 2022

Received: 25 October 2021 / **Revised:** 18 December 2021 / **Accepted:** 28 December 2021

ABSTRACT

Nanostructured silicon and silicon-aluminum compounds are synthesized by a novel synthesis strategy based on spark plasma sintering (SPS) of silicon nanopowder, mesoporous silicon (pSi), and aluminum nanopowder. The interplay of metal-assisted crystallization and inherent porosity is exploited to largely suppress thermal conductivity. Morphology and temperature-dependent thermal conductivity studies allow us to elucidate the impact of porosity and nanostructure on the macroscopic heat transport. Analytic electron microscopy along with quantitative image analysis is applied to characterize the sample morphology in terms of domain size and interpore distance distributions. We demonstrate that nanostructured domains and high porosity can be maintained in densified mesoporous silicon samples. In contrast, strong grain growth is observed for sintered nanopowders under similar sintering conditions. We observe that aluminum agglomerations induce local grain growth, while aluminum diffusion is observed in porous silicon and dispersed nanoparticles. A detailed analysis of the measured thermal conductivity between 300 and 773 K allows us to distinguish the effect of reduced thermal conductivity caused by porosity from the reduction induced by phonon scattering at nanosized domains. With a modified Landauer/Lundstrom approach the relative thermal conductivity and the scattering length are extracted. The relative thermal conductivity confirms the applicability of Kirkpatrick's effective medium theory. The extracted scattering lengths are in excellent agreement with the harmonic mean of log-normal distributed domain sizes and the interpore distances combined by Matthiessen's rule.

KEYWORDS

thermal conductivity, mesoporous silicon, porosity, spark plasma sintering, nanoscale modeling

1 Introduction

Reducing the thermal conductivity of technologically relevant materials is mandatory for a manifold of applications to improve device-related thermal management capabilities or to optimize energy-conversion functionality as for example in thermoelectric devices. Among the most promising routes to achieve low thermal conductivity are nanostructuring approaches [1–3] next to porosification [4–6]. While a combination of these strategies seems most natural, a quantitative understanding of the thermal conductivity remains challenging in composite systems in which grain boundaries and pores coexist. Due to reduced phonon mean free paths, these systems are expected to show a suppressed thermal conductivity if grain sizes and interpore distances cover comparable length scales in the range of several nanometers. However, separating the underlying effects is a formidable task.

Tackling this challenge, we have chosen to study nanostructured porous silicon, which is a prominent model system, to investigate thermal transport at the nanoscale from a fundamental point of view. The model system status is justified because of the well-known crystal structure, resulting phonon dispersion, and thermal properties, which have been measured and theoretically modeled for decades. On the other hand, silicon is a prominent candidate that is abundant, non-toxic and, due to its ubiquity, comes along with well-established industrial processes [7]. While the thermal conductivity of bulk silicon [8] is far too large for applications demanding thermally insulating properties, nanostructured silicon is an excellent candidate that is of immediate technological relevance. Tons of waste silicon from the kerf of the semiconductor industry [9] and defective solar cells are potential base materials for thermoelectric applications. Such silicon thermoelectric generators have been demonstrated as micro devices [10, 11] and high-temperature modules [12] benefiting from the advanced level of silicon technology. However, to be useful in a competitive application, a fundamental understanding of the underlying heat transport mechanisms must be achieved in order to guide further material optimization.

Recent efforts succeeded to improve the thermoelectric performance in silicon-based devices by a strong reduction of the thermal conductivity [13]. A reduced thermal conductivity was observed in nanostructured bulk silicon [9, 14–18], holey ribbons [19], porous silicon [20], nanowires [21–24] as well as in isotopically controlled silicon nanostructures [25]. Neutron

Address correspondence to danny.kojda+NARE@gmail.com

scattering on single crystalline nanostructured mesoporous silicon (pSi) provided direct microscopic evidence that the elastic properties and therefore the phonon group velocity remain essentially unchanged compared to bulk single crystalline silicon and cannot explain the reduced thermal conductivity [26, 27]. As possible quantum confinement effects do not modify the phonon dispersion relation down to 10 nm [27], the reduction of the thermal conductivity in silicon most likely originates in the reduction of the phonon mean free path.

In bulk single crystalline silicon impurity scattering, boundary scattering and Umklapp scattering are the main temperature-dependent mechanisms limiting the phonon mean free path [8]. For single crystalline silicon nanowires and thin films, the thermal conductivity is substantially decreased due to increased surface scattering that also depends on surface roughness [22, 24]. Grain boundary scattering is identified as main mechanism for the reduction of thermal conductivity in polycrystalline nanostructured bulk silicon [9, 17]. The materials studied in our work are polycrystalline nanostructured Si bulk samples with extensive inner surfaces, which are given by the pore distribution. Hence, the thermal conductivity is strongly dominated by both, grain boundary scattering and surface scattering at the pores.

In this study, a novel synthesis strategy for nanostructured Si bulk samples with high porosity is demonstrated by spark plasma sintering (SPS) of mesoporous silicon. We investigate the nanostructure, porosity, and thermal conductivity of sintered silicon synthesized from silicon nanopowder, crushed pSi, and nanostructured aluminum as additive. The motivation to use pSi as base material is to start with a material of high well-defined intrinsic porosity. In contrast, the nanopowder's initial porosity can depend on mixing and drying conditions. Further, as pSi is made of silicon wafers, the base material's purity and doping are well-defined and controllable for further optimization. At the time of this study, the purity of wafer grade silicon (9N) is much higher than of commercially available Si-nanopowders (2N), that may be refined by extra steps [28].

Aluminum affects the grain growth due to the reduced melting point of the binary silicon-aluminum system [29]. A reduced melting point of this system is also reported as metal-induced crystallization (MIC) in thin film fabrication [30]. Our material interfaces consisting of silicon-alumina and/or silicon-aluminum are very similar to the sputtered layers for MIC, so that similar processes to MIC may appear during ramping to the final temperature that for our experiments is much higher than for MIC. Using sinter temperatures higher than 1,000 °C the aluminum will melt, allow Si particles to glide, likely fill inter-particle gaps during compaction and give mechanical stability to the structure after cooldown as known from liquid phase sintering by SPS [31].

After cooldown of the hypereutectic silicon-aluminum system, the observation of individual silicon grains and eutectic phase solidification is expected. The microstructures of near eutectic compositions containing about 12.6% silicon are well characterized and exhibit lamellar structures that could introduce additional grain boundaries [32]. The structure of the alloyed hypereutectic Al-50Si has grain sizes of several micrometers [33]. The microstructures of higher silicon concentrations, as used in our study, are not yet reported. Since our silicon concentration is far from the eutectic concentration, a small amount of the eutectic could occur, but is not observed in the samples after the SPS.

For nanostructure characterization, quantitative analysis is applied to images obtained by scanning electron microscopy (SEM). We demonstrate that the morphology of spark-plasma-densified binary silicon-aluminum nanomaterials can be modified to a large extent by the aluminum concentration, the dispersion method, and sinter conditions. We employ advanced image processing algorithms adapted to our specific task aiming at unambiguously characterizing the sample morphology in terms of domain size and interpore distance distributions. This analysis plays a key role to confirm the results of the entirely different and thus complementary thermal conductivity analysis. In the latter, the contributions of the porosity and the nanostructure to drastically reduce the thermal conductivity of the nanocomposites are separated by applying a modified Landauer/Lundstrom approach to our multi-parameter-dependent thermal conductivity data. With this quantitative model, the temperature-dependent reduction of the thermal conductivity caused by porosity can be disentangled and analyzed separately from the effect of the nanostructure. In particular, we show that the mean free path, which is treated as free fit parameter in the modified Landauer/Lundstrom model, is in excellent agreement with the effective domain size from SEM analysis over a large range of length scales extending from 7 nm to 1 μm. In addition, we find that the dependence of the thermal conductivity on sample porosity is well described by the effective medium model put forward by Kirkpatrick [34–36].

2 Experimental

2.1 Sample preparation

Weighing-in of silicon nanopowder (99%, particle size: < 100 nm, supplier: Sigma-Aldrich) and aluminum nanopowder (99.9%, particle size: 18 nm, supplier: Ionic Liquids Technologies GmbH) with aluminum contents up to 20 wt.% were performed in inert atmosphere. Subsequently, oxygen-free solvents were added to the nanopowder mixtures, using either pentane (C_5H_{12}) or octane (C_8H_{18}). The homogenization of the nanoparticles was performed in gas-tight bottles in an ultra-sonic bath (USB) outside the inert atmosphere for 1 h and by ultra-sonic dispersion (USD) for 3 × 15 s with a UP200Ht homogenizer (Hielscher Ultrasonics GmbH) in inert atmosphere. For USD, C_8H_{18} was used as dispersant because its higher boiling point results in a better energy intake. The dispersions were vacuum dried and filled into Ø12.7 mm graphite dies covered with graphite foil.

To obtain silicon powder of high purity and well-defined initial porosity as base material for the SPS, pSi of different porosity was prepared from boron doped wafers by a two-step electrochemical etching process [26, 37]. To vary the initial porosity different wafer resistivity and different electrolyte concentrations were used. The wafers' specification, etching and membrane detaching conditions are summarized in Table 1 and sketched in Fig. S5 in the Electronic Supplementary Material (ESM). For wafer types I and III a two-step processing was chosen resulting in freestanding membranes with a thickness of 380 μm (Fig. S5(a) in the ESM). To scale up the powder production, silicon wafers of 1,500 μm thickness were used (types II and IV). The wafer of type II was etched from both sides with a residual silicon layer of about 20 μm (Fig. S5(b) in the ESM). The pSi of wafer type IV self-detached during the etching after the given time resulting in a 500 μm thick membrane (Fig. S5(c) in the ESM).

After pSi synthesis, the membranes were flushed with water, rinsed in hydrofluoric acid (HF) for 2 min to remove surface oxides, and finally rinsed 3 × 2 min in dry C_8H_{18}. The sample within the last C_8H_{18} bath was transferred into the glovebox and the membrane was dried in inert atmosphere. Herein, the membranes were powdered in an agate mortar and filled into graphite dies, as described above.

For pSi 18 nm aluminum nanopowder was added during the mortaring (MOR). As an alternative aluminum source, a 100 nm

Table 1 Different doping and electrolyte concentrations are used to vary the initial porosity of the silicon starting material. Thick wafers are used to increase the powder yield. Electrolyte ratios are given volumetric. The porosities of the as-etched membranes were measured by nitrogen sorption isotherms

Wafer type	I	II	III	IV
Thickness (μm)	380	1,500	380	1,500
Resistivity (Ω/cm)	0.01	0.01	0.001	0.01
Etching:				
HF (48%):ethanol	4:6	8:2	7:1	4:6
Time (min)	400	2 × 1,155	60	830
Current density (mA/cm²)	10.2	10.2	150	10.2
Detaching:				
HF (48%):ethanol	4:6	—	1:1	—
Time (s)	40	—	120	—
Current density (mA/cm²)	121.8	—	213	—
As-etched porosity	70%	53%	84%	79%

thick aluminum film was sputtered on top of freestanding membranes before MOR. To minimize the oxygen contamination, the samples were handled in inert atmosphere all time.

All powders were compacted by SPS [38] in a FCT HP D10-GB system (FCT Systeme GmbH). This system combines a SPS furnace with a glovebox. We emphasize, that all powder preparation was performed in the absence of air or moisture in order to reduce the effect of possible surface oxides during the synthesis. The samples were densified in vacuum at an uniaxial pressure of 34 MPa at 1,000 and 1,200 °C and with holding times of 5 and 10 min. Details on the experimental conditions are summarized in Section S5 and in Table S1 in the ESM. The graphite foil was removed by sandblasting and grinding. The samples were high-end polished to allow for visualization of the nanostructure by SEM.

2.2 Characterization methods

The specimen mass and its volume including pore voids provide the apparent density ρ_b. The enveloping surface and thus the volume of nonuniform samples were determined from optical microscope images using chroma keying and thickness measurements. The porosity Φ of a specimen is determined by

$$\Phi = 1 - \frac{\rho_b}{\rho_t} \quad (1)$$

with $\rho_t = c_{Si}\rho_{Si} + c_{Al}\rho_{Al}$ the theoretical density and c_{Si} and c_{Al} the mass fractions of the silicon aluminum composite. The densities of the solid materials are $\rho_{Si} = 2.336$ g/cm³ and $\rho_{Al} = 2.6878$ g/cm³.

The samples' morphology and chemical composition were investigated by SEM and simultaneous energy dispersive X-ray spectroscopy (EDX) with a LEO GEMINI 1530 UltraPlus (Zeiss) on high-end polished surfaces. The channeling contrast obtained at 5 kV, largest aperture, high-current mode, and highest contrast settings allow to image individual grains of the nanostructured bulk material.

The microscopic chemical composition was analyzed with two-dimensional (2D) micro X-ray fluorescence (XRF) in a M4 TORNADO setup (Bruker Corporation) with a spatial resolution of 25 μm. At the center of the sample, 2.5 mm × 2.5 mm maps were taken with a resolution of 300 × 300 points and a dwell time of 2 ms.

Temperature-dependent thermal diffusivity D was measured with the LFA 457 MicroFlash (NETZSCH-Gerätebau GmbH) in the temperature range between 300 and 773 K. The effective thermal conductivity was calculated by $\lambda_{eff} = \rho_b C_p D$, with ρ_b the measured apparent density and C_p the specific heat capacity.

3 Results

3.1 Sample morphology and porosity

3.1.1 *Powder processed samples*

Domain size distributions and interpore distance distributions are extracted from SEM images as described in Section S1 in the ESM. We find that the domain sizes are well described with log-normal distributions while interpore distances show Γ-distributions. The arithmetic mean of the domain size distribution $\Lambda_{mean,SEM}$ is used to discuss domain size compared to the averaged particle size of the original powder. Figure 1 summarizes the sample morphologies described by porosity Φ and domain size $\Lambda_{mean,SEM}$ for sintered powder and pSi samples. The aluminum concentration, synthesis conditions, and morphological classification are encoded by color, symbol filling, and symbol shape.

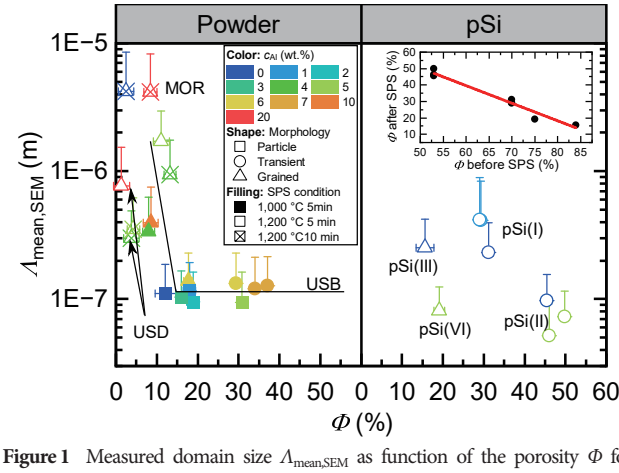

Figure 1 Measured domain size $\Lambda_{mean,SEM}$ as function of the porosity Φ for samples processed from nanopowders and pSi. The aluminum concentration is color coded, the symbol filling gives the main process parameters. The symbol shape describes the sample morphology as determined by SEM images of highly polished samples. The powder mixing procedures are indicated as USB, USD, and MOR. The solid line is a guide to the eye for samples mixed by USB. The inset compares the porosity of the pSi before and after the SPS process showing a linear dependency.

We observe that powder samples sintered at 1,000 °C (Fig. 1 (left), solid filling) span a porosity range from 9% to 37%. Samples with aluminum concentration c_{Al} < 5% show a morphology comprising individual particles (square symbols) with initial neck growth, a fine pore structure, and a domain size consistent with the initial particle size (Fig. 2(a)).

Aluminum concentrations in the range 5% ≤ c_{Al} < 10% cause slightly larger domain sizes, larger pores and larger interpore distances (compare Fig. 2(b) vs. Fig. 2(a) and Fig. 1). Particles melt together leaving larger pores compared to samples with low aluminum concentrations. We label this morphology as transient state because it cannot clearly be classified as particle-like or grain-like structure (circle symbols). Among powder-sintered samples, these samples have highest porosity. The high porosity compared to particle-like morphology is unexpected, as the transient samples show stronger grain growth that should lead to better compactability. Possible origins may be a lower tap density of the dried initial powders or a lower sinter temperature at the sample position that could be caused by temperature gradients along the die and a slightly off-center position of the sample in the die.

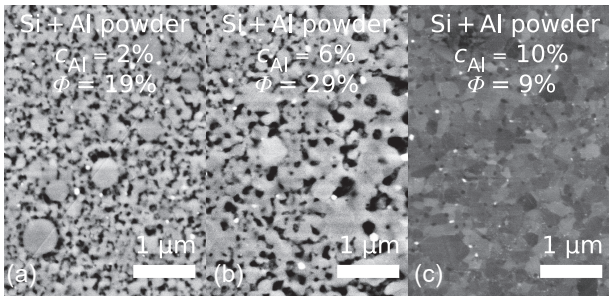

Figure 2 SEM images of a selection of powder-processed samples sintered at 1,200 °C. The aluminum concentration increases from (a) to (c). Silicon (gray) includes pores (black) with irregular shape (a) and (b) and round shape (c). The bright particles (white) remain from the last polishing step and are made of silicon as evidenced by EDX. On the length scale shown here, aluminum agglomerations were not observed.

Aluminum concentrations above 10% lead to grain growth and reduction of the porosity. These samples show grained (triangle symbols in Fig. 1), polycrystalline morphology with a mean domain size of about 400 nm and a low porosity of 9% (Fig. 2(c)). As additional proof for aluminum-induced grain growth, large silicon grains are found around an aluminum agglomeration (Fig. S3(a) in the ESM).

Sintering at 1,200 °C leads to strong grain growth. All powder samples sintered at 1,200 °C (open and crossed symbols) show a grained morphology with domain sizes ranging from 300 nm to 4 µm and a porosity $\Phi \leq 13\%$. The reduced porosity shows that particle densification and/or pore migration to the outside of the sample is more efficient. However, some macro pores remain in the polycrystalline matrix as shown in Fig. 3(a). The round shape of the pores indicates liquification of silicon during the sintering [39].

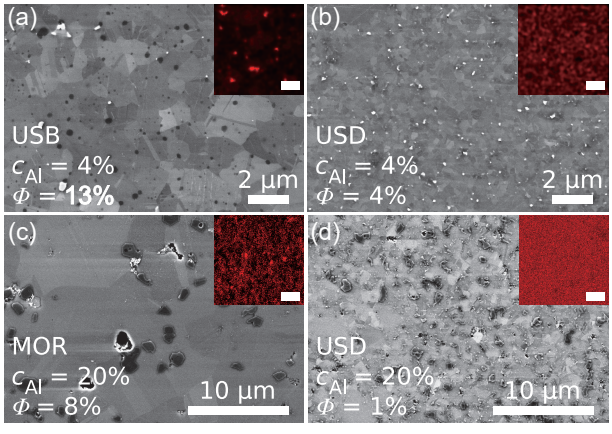

Figure 3 Influence of the mixing method on the microstructure and aluminum distribution. Gray areas are silicon, black areas with white corona represent aluminum agglomerations, purely black areas are pores with mainly round shape (a) and irregular shape (c) and bright particles (white) remain from the last polishing step. The insets show X-ray fluorescent maps of the lateral aluminum distribution (scale bar: 500 µm). Best homogeneity is reached by USD.

The initial particle distribution has significant impact on the final morphology. Figure 3 reveals the effect of different powder mixing methods on the resulting aluminum distributions and on the microstructure. Samples mixed by USD show lower porosity, smaller domain sizes, more homogeneous aluminum concentration, and smaller aluminum precipitates compared to samples mixed by USB or MOR (Fig. 3(a) vs. Fig. 3(b) and Fig. 3(c) vs. Fig. 3(d)). XRF on the millimeter scale (Fig. 3 insets) indicates aluminum agglomerates for USB mixed samples. In contrast, a uniform composition is achieved by MOR and USD.

The expected lamellar and/or fine structured features from eutectic solidification are not observed in our samples. The microstructure that we observe for $c_{Al} \leq 10\%$ consists of silicon grains and pores. For samples with $c_{Al} = 20\%$, individual round-shaped Al agglomerations were identified (Figs. 3(c) and 3(d)). Our micro structure analysis does not provide a stringent proof for grains that originate from the hypereutectic growth, but most likely from crystallization of individual particles of the base material. The lack of eutectic features may be related to the short processing times and rapid temperature changes by SPS, which are known to preserve the nanostructure of the base materials.

3.1.2 *Mesoporous silicon processed samples*

Sintered pSi samples are up to 52% porous and domain sizes range from 50 to 400 nm even though sintered with 1,200 °C (Fig. 1 (right)). Thus, pSi samples show higher porosity and lower domain size compared to powder processed samples sintered with comparable conditions. The main difference is that individual nanoparticles of the powders can easily move against each other during the compaction, while the crushed pSi consists of micrometer sized particles that contain a dense mesoporous network in a rigid single crystalline system. Therefore, the stability of the pSi system with respect to external pressure and temperature determines the resulting porosity.

The inset of Fig. 1 compares the porosity of pSi samples before and after SPS. The post-SPS porosity decreases with increasing initial pSi porosity. This behavior can be understood as increasing porosity goes along with decreasing fracture toughness. The analysis of the relative piston position as function of temperature in Fig. S4 in the ESM confirms that samples of high initial porosity are densified by pressure rather than by temperature.

Figure 4 exhibits the microstructure of sintered pSi samples. In the following, we use the nomenclature pSi(I) to pSi(IV) to indicate the pSi base material and the process route by use of the Roman numerals equivalently used for the wafer type. The open pore network of samples made from pSi(I) and pSi(II) compares with sintered powder samples in the transient state.

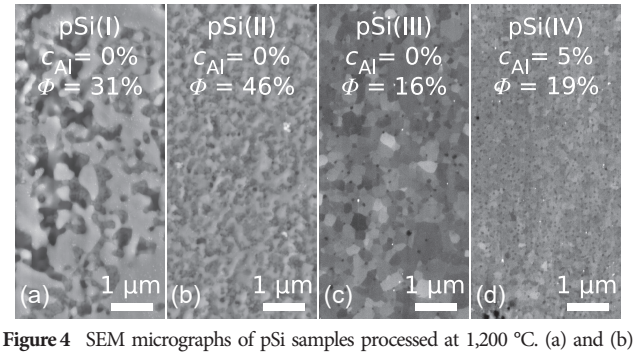

Figure 4 SEM micrographs of pSi samples processed at 1,200 °C. (a) and (b) Bright gray contrasts represent silicon in the polished plane. The pore network is shown by dark gray to black contrasts. (c) and (d) Individual grains (bright gray to dark gray contrast) embed circular pores (black contrast). The microstructure is mainly determined by the initial porosity that is 70%, 53%, 84%, and 79% for pSi(I) to pSi(IV).

Samples made from pSi(II) show the lowest relative change of porosity before and after the SPS as well as no significant change to the nanostructure of as-grown pSi. In contrast nano-grained facets that embed spherical pores grow in samples made from pSi(III) and pSi(IV). Here, the grain growth may be favored due to better energy intake on the collapsed and compacted host network due to the high initial porosity.

For pSi(I) the additional aluminum is added by a sputtered aluminum film before crushing the membrane. Due to the aluminum, the densification onset is decreased from 1,000 to 800 °C

(Fig. S4 in the ESM). The sinter results have a higher domain size and lower porosity in agreement with sintered powder samples (Fig. 1).

The pSi(II) samples with 5% aluminum powder mixed by USD and MOR do not significantly change their morphology and porosity. The compaction onset for all pSi(II) samples, with and without aluminum, is around 1,100 °C which is much higher than for the other pSi samples (Fig. S4 in the ESM).

The onset of the compaction at higher temperature may be related to the high fracture toughness given by the lowest pre-SPS porosity. Surprisingly, EDX reveals that the aluminum diffused around the individual micrometer sized grains. The diffusion depth of 3 μm (Fig. S3(b) in the ESM) is in agreement with the expected diffusion length of aluminum in silicon for the applied synthesis conditions [40]. We see the applied USD as main reason for this observation, as the mortared reference sample does not show aluminum surrounded grains. USD leads to the homogeneous particle distribution around individual grains. However, it remains an open question why diffusion is seen instead of increased grain growth.

3.2 Temperature-dependent thermal conductivity

The quantitative analysis of porous materials' thermal conductivity is challenging because voids and grains are part of the nanostructure and simultaneously reduce the macroscopic effective thermal conductivity λ_{eff}. We follow the approach to separate the effective thermal conductivity by $\lambda_{eff} = \lambda_0\lambda_r$ [41]. λ_0 is the intrinsic thermal conductivity of the dense material that depends on the grain size. The relative thermal conductivity $0 \le \lambda_r \le 1$ is a function of porosity Φ [41].

Different models for the relative conductivities have been put forward in the past [36, 41, 42]. The simple models only include the porosity Φ [41], while recently developed models include pore size distribution, pore shape, pore randomization, and surface properties [43, 44].

Figure 5 classifies the temperature-dependent λ_{eff} of powder processed samples according to maximum sinter temperature, porosity, aluminum concentration, morphology, and mixing method. Porosity and microstructure vary from sample to sample. Consequently, a cross-sample comparison of λ_{eff} is challenging. However, general trends are evident.

The thermal conductivities of powder samples with particle or transient morphology are lower than for grained morphology. Thus, almost all samples sintered at 1,000 °C have a smaller λ_{eff} than samples sintered at 1,200 °C. This behavior is expected, as higher sinter temperatures yield lower porosity and larger domain sizes (Fig. 1). Taking samples with particle and transient morphology into account, an increasing Φ results in a decreasing λ_{eff}. As particle and transient samples have a similar domain sizes, this reduction is attributed within the framework of our model $\lambda_{eff} = \lambda_0\lambda_r$ to the increased porosity. As discussed below (Eq. (2)), λ_0 only depends on the domain size whereas λ_r depends on the porosity.

The thermal conductivity of grained samples synthesized at 1,000 °C with c_{Al} = 4% and 10% compare with USD mixed samples sintered at 1,200 °C. This can be explained by similarities in domain size and porosity (Fig. 1).

The samples sintered at 1,200 °C and mixed by USD show lower thermal conductivities than samples synthesized by mixing methods other than USD. As the Φ of USD mixed samples is lower than for the others, the mixing procedure indirectly influences the thermal conductivity by modification of the nanostructure. Grain sizes are smaller in USD samples (Figs. 1, 3(c) and 3(d)), so that the lower thermal conductivity is explained by the reduced domain size.

The highest effective thermal conductivity at all temperatures was observed for the sample of largest grains and lowest porosity made of the pure silicon powder.

The effective thermal conductivity of sintered pSi samples (Fig. 6), even though sintered at 1,200 °C, is lower than of identically sintered silicon powder samples. The thermal conductivities' dependence on porosity cannot be explained by the nanostructure alone (Figs. 4 and 6). The combination of both, high porosity and small domain size results in the lowest thermal conductivity for pSi(II)-samples. As previously discussed, sintered pSi(II) samples almost preserved the micro and nanostructure also with aluminum present.

4 Discussion

4.1 Relative thermal conductivity and phonon mean free path

In order to decouple the effect of porosity and the domain size, λ_{eff} is fitted with a modified Landauer/Lundstrom model [45, 46] given by

$$\lambda_{eff}(T) = \lambda_r\lambda_0 = \lambda_r\left(\frac{k_B^2\pi}{6}T\right)\int_0^{\omega_0}\frac{4}{3}\Lambda(\omega)M_{ph}(\omega)W_{ph}(\omega)d\omega \quad (2)$$

with the relative thermal conductivity λ_r, the lattice temperature T, the frequency dependent phonon mean free path $\Lambda(\omega)$, the number of modes $M_{ph}(\omega)$, and the window function $W_{ph}(\omega)$.

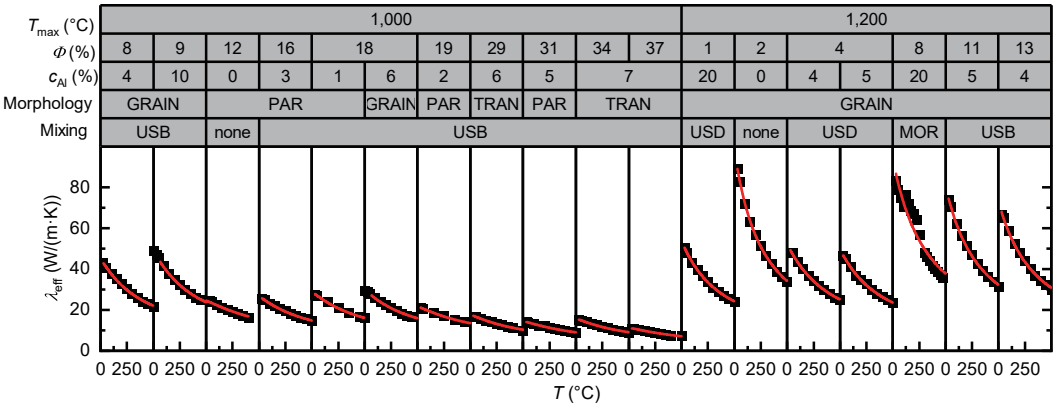

Figure 5 Effective thermal conductivity λ_{eff} as function of temperature for sintered powder samples. The samples are grouped together by the maximum sinter temperature T_{max} and ordered by increasing porosity Φ and increasing aluminum concentration c_{Al}. Morphology (grained (GRAIN), particle (PAR), and transient (TRAN)) and the mixing method (USB, USD, and MOR) are indicated. Red solid lines represent non-linear least square fits applying the model described in Section S2 in the ESM with λ_r and Λ_D as the only free parameters.

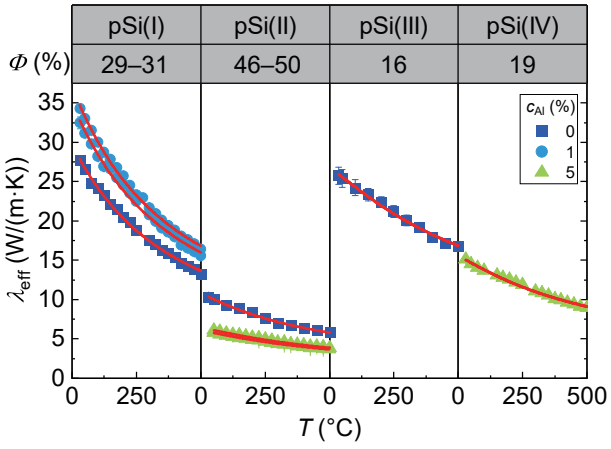

Figure 6 The effective thermal conductivity of sintered pSi. Red solid lines represent non-linear least square fits applying the model in Section S2 in the ESM.

Details about the frequency-dependent terms are given in Section S2 in the ESM.

For fitting, the only free parameters are the relative thermal conductivity λ_r and the phonon mean free path Λ_D. As evident in Figs. 5 and 6 these non-linear least square fits describe the measured thermal conductivity very well.

The extracted relative thermal conductivity λ_r is shown as function of the porosity Φ in Fig. 7(a). Values with a porosity below 15% scatter heavily. Taking data of $\Phi > 15\%$ into account the effective medium models by Lewis–Nielsen [47] and Kirkpatrick [36] describe λ_r well. In contrast, the classical models given by Maxwell, Rayleigh, or Bruggemann [47] fail to describe our data.

The obtained parameters of the Lewis–Nielsen model are the maximum packing fraction $\Phi_m = 20\%$ and the shape coefficient $A = 3.83$. The maximum pore filling fraction of 20% underestimates our observed maximum porosity and thus queries the application of this model.

For the Kirkpatrick model, our data gives a thermal percolation threshold $\Phi_c = 60\%$. This is comparable to the percolation threshold of 57% found in electrical transport studies in pSi [48].

One observes excellent agreement between $\Lambda_{D,fit}$ and the effective domain size $\Lambda_{eff,SEM}$ (Fig. 7(b)). This is extraordinary as both originate from two fundamentally different characterization methods, that are the analysis of the temperature-dependent conductivity and quantitative image analysis. $\Lambda_{eff,SEM}$ is calculated by

$$\Lambda_{eff,SEM}^{-1} = \Lambda_{D,SEM}^{-1} + \Lambda_{pore,SEM}^{-1} \quad (3)$$

As demanded by Matthiessen's rule for independent scattering channels $\Lambda_{pore,SEM}$ and $\Lambda_{D,SEM}$ are taken as the harmonic means of the interpore distance distribution and domain size distribution [49, 50]. Neglecting scattering at pores ($\Lambda_{pore,SEM}^{-1} = 0$) results in a shift from the identity (gray points in Fig. 7(b)), proving this is an oversimplification.

4.2 The intrinsic thermal conductivity

λ_0 is predicted by the original Landauer/Lundstrom model. For $T = 300$ K, Fig. 8 exhibits $\lambda_0(\Lambda)$ based on the Landauer/Lundstrom model (red curve), that is in exceptional agreement with $\lambda_0(\Lambda_{D,fit}) = \lambda_{eff}/\lambda_r$, the data found within this study (black squares). In Fig. 8, we add data from as-etched pSi and a size-dependent estimation from de Boor [51]. He used a simple parallel thermal resistance model ($\lambda_0 = \lambda_{eff}/(1 - \Phi)$) for the effect of porosity and considered the structure size d as the relevant scattering length. The deviation (green symbols and line) from our data can be easily resolved (blue stars) by consideration of the here found relative thermal conductivity relation (Fig. 7) and a scattering length given by the structure size and pore distance. We cannot translate all data points from de Boor [51] because of missing geometric data or $\Phi \geq 0.6$ for which the effective medium model fails.

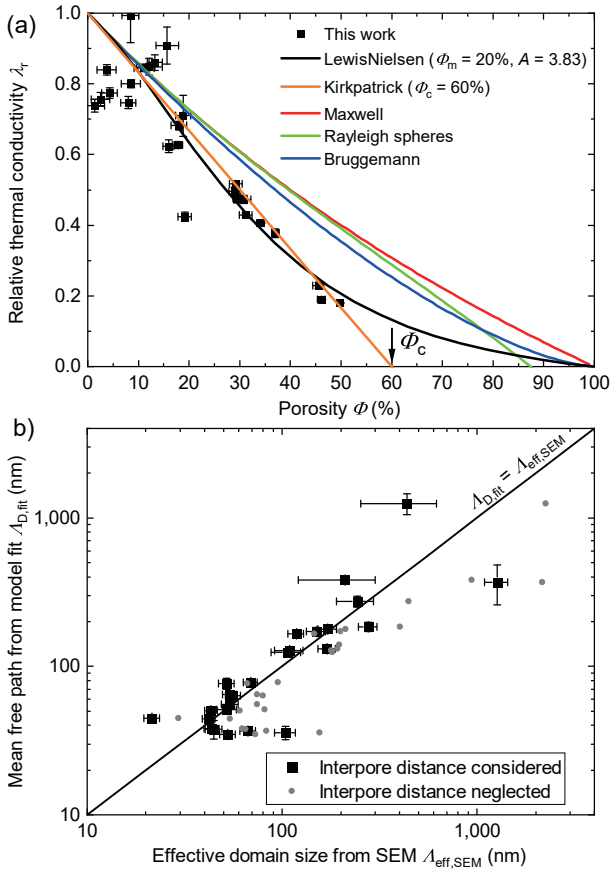

Figure 7 (a) Extracted relative thermal conductivity λ_r as function of the porosity Φ is compared to the Maxwell model (red), the Rayleigh model for spherical pores (green), the Bruggemann model (blue), the Lewis–Nielsen model (black), and the Kirkpatrick model (orange). (b) Mean free path $\Lambda_{D,fit}$ extracted from fitting the temperature-dependent effective thermal conductivity as function of the effective domain size $\Lambda_{eff,SEM}$. Gray points show the mean free path only taking the domain size into account. The solid line shows the identity $\Lambda_{D,fit} = \Lambda_{eff,SEM}$.

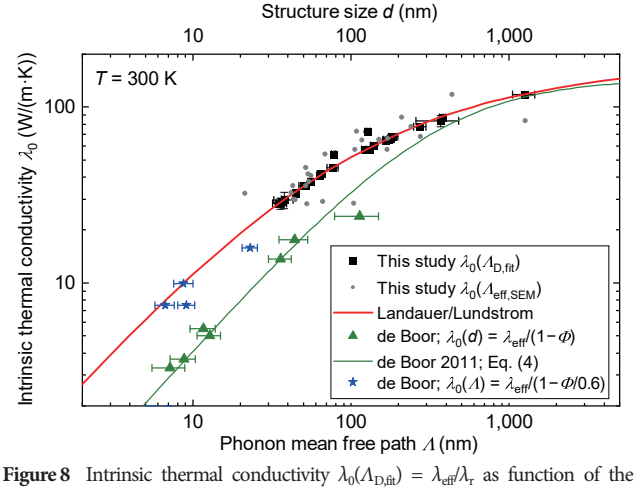

Figure 8 Intrinsic thermal conductivity $\lambda_0(\Lambda_{D,fit}) = \lambda_{eff}/\lambda_r$ as function of the mean free path $\Lambda_{D,fit}$ and the modified Landauer/Lundstrom model of this study. Literature data of de Boor [51] (green points and line) are in agreement with our model considering the here found relative thermal conductivity relation and the effective mean free path of the structure and interpore distance (blue stars).

4.3 Model assumptions and applicability

The basic assumption in Eq. (3) is the separability of λ_{eff} for contributions due to porosity and different phonon scattering mechanisms in the nanostructured samples. The porosity-dependent part is treated within the framework of well-established effective medium models [36]. The phonon scattering dependent part is treated within the model of Landauer/Lundstrom [46]. The latter assumes the existence of different scattering channels, like boundary scattering, impurity scattering, Umklapp scattering, scattering at nanosized domains, and the applicability of Matthiessen's rule.

On a technical note, the main assumption about separability is not unprecedented [52]. One might even consider it as a necessity to conceive a tractable analytical model. Similarly, the application of Matthiessen's rule is a helpful simplification. Like any theoretical model, these and other assumptions obviously can find their justification in different ways. Of course, a comparison with *ab initio* calculations of the thermal conductivity with our model is desirable, but clearly beyond the scope of this experimental work. However, we consider equally convincing the excellent agreement between $\Lambda_{eff,SEM,}$ and $\Lambda_{D,fit}$ as a valid experimental justification for our approach. Finally, our model allows to describe the thermal conductivity for porous silicon samples in the porosity range $0 \leq \Phi \leq 0.6$ and mean free paths $\Lambda \geq 7$ nm.

5 Conclusions

In summary, we have presented a detailed study of the thermal conductivity of spark plasma synthesized porous nanostructured silicon and silicon-aluminum compounds with well characterized porosity, domain size, and interpore distance distributions. Our synthesis strategy to prepare nanostructured bulk monoliths of silicon employs metal-assisted crystallization in bulk samples and builds on the porosity inherent to the nanoporous starting material prior to SPS. Quantitative SEM image analysis demonstrates morphology control of spark plasma sintered binary silicon-aluminum nanomaterials synthesized by different USD methodologies. Since the high porosity is maintained after SPS processing and excessive grain growth is suppressed, both, nanostructure and porosity simultaneously lead to a strong reduction of thermal conductivity. Temperature-dependent measurements allow to disentangle the effect of porosity and size effects to explain the reduction of the thermal conductivity compared to bulk. The proposed model, a modified Landauer/Lundstrom model incorporating the porosity, describes the temperature-dependent thermal conductivity as function of the porosity, domain size, and temperature for effective mean free paths ranging between 7 nm and 1 μm and porosities up to 60%. The model is applicable to a broad range of materials based on porous nanomaterials beyond the specific material system studied in the present work. Due to the close correspondence of heat transport by phonons to charge carrier transport, the proposed model provides a pathway to a thorough understanding of electronic transport in porous nanostructured material systems as well.

Acknowledgements

The authors gratefully acknowledge support of the Helmholtz Energy Materials Foundry (HEMF). This research was supported in part by Deutsche Forschungsgemeinschaft (DFG) (No. 402553194/for Natalia Gostkowska-Lekner). We thank D. Abou-Ras (HZB) and L. Steinkopf (HZB) for access to the SEM and XRF facilities. We thank A. Schulz (BAM) for ICP-SF-MS on the aluminum nanopowder and A. Steigert (HZB) for preparation of Al films on pSi membranes.

Funding note: Open access funding provided by Helmholtz-Zentrum Berlin für Materialien und Energie GmbH.

Electronic Supplementary Material: Supplementary material (quantitative image analysis, Landauer/Lundstrom model details, densification curves, and experimental parameters) is available in the online version of this article at https://doi.org/10.1007/s12274-022-4123-y.

Open Access This article is licensed under a Creative Commons Attribution 4.0 International License, which permits use, sharing, adaptation, distribution and reproduction in any medium or format, as long as you give appropriate credit to the original author(s) and the source, provide a link to the Creative Commons licence, and indicate if changes were made.

The images or other third party material in this article are included in the article's Creative Commons licence, unless indicated otherwise in a credit line to the material. If material is not included in the article's Creative Commons licence and your intended use is not permitted by statutory regulation or exceeds the permitted use, you will need to obtain permission directly from the copyright holder.

To view a copy of this licence, visit http://creativecommons.org/licenses/by/4.0/.

References

[1] Snyder, G. J.; Toberer, E. S. Complex thermoelectric materials. *Nat. Mater.* **2008**, *7*, 105–114.

[2] Alam, H.; Ramakrishna, S. A review on the enhancement of figure of merit from bulk to nano-thermoelectric materials. *Nano Energy* **2013**, *2*, 190–212.

[3] Qian, X.; Zhou, J. W.; Chen, G. Phonon-engineered extreme thermal conductivity materials. *Nat. Mater.* **2021**, *20*, 1188–1202.

[4] Xie, G. F.; Ju, Z. F.; Zhou, K. K.; Wei, X. L.; Guo, Z. X.; Cai, Y. Q.; Zhang, G. Ultra-low thermal conductivity of two-dimensional phononic crystals in the incoherent regime. *npj Comput. Mater.* **2018**, *4*, 21.

[5] He, P. L.; Wu, Y. Constructing of highly porous thermoelectric structures with improved thermoelectric performance. *Nano Res.* **2021**, *14*, 3608–3615.

[6] Hofmann, T. Nanostructured energy materials: From organic photovoltaic to hybrid thermoelectrics. In *Soft Matter and Biomaterials on the Nanoscale*; Huber, P., Ed.; World Scientific: Singapore, 2020; pp 435–479.

[7] Beretta, D.; Neophytou, N.; Hodges, J. M.; Kanatzidis, M. G.; Narducci, D.; Martin-Gonzalez, M.; Beekman, M.; Balke, B.; Cerretti, G.; Tremel, W. Thermoelectrics: From history, a window to the future. *Mater. Sci. Eng. :R:Rep.* **2019**, *138*, 100501.

[8] Glassbrenner, C. J.; Slack, G. A. Thermal conductivity of silicon and germanium from 3 °K to the melting point. *Phys. Rev.* **1964**, *134*, A1058–A1069.

[9] He, R.; Heyn, W.; Thiel, F.; Pérez, N.; Damm, C.; Pohl, D.; Rellinghaus, B.; Reimann, C.; Beier, M.; Friedrich, J. et al. Thermoelectric properties of silicon and recycled silicon sawing waste. *J. Mater.* **2019**, *5*, 15–33.

[10] Perez-Marín, A. P.; Lopeandía, A. F.; Abad, L.; Ferrando-Villaba, P.; Garcia, G.; Lopez, A. M.; Muñoz-Pascual, F. X.; Rodríguez-Viejo, J. Micropower thermoelectric generator from thin Si membranes. *Nano Energy* **2014**, *4*, 73–80.

[11] Noyan, I. D.; Dolcet, M.; Salleras, M.; Stranz, A.; Calaza, C.; Gadea, G.; Pacios, M.; Morata, A.; Tarancon, A.; Fonseca, L. All-silicon thermoelectric micro/nanogenerator including a heat exchanger for harvesting applications. *J. Power Sources* **2019**, *413*, 125–133.

[12] Kessler, V.; Gautam, D.; Hülser, T.; Spree, M.; Theissmann, R.; Winterer, M.; Wiggers, H.; Schierning, G.; Schmechel, R. Thermoelectric properties of nanocrystalline silicon from a scaled-up synthesis plant. *Adv. Eng. Mater.* **2013**, *15*, 379–385.

[13] Elyamny, S.; Dimaggio, E.; Magagna, S.; Narducci, D.; Pennelli, G.

High power thermoelectric generator based on vertical silicon nanowires. *Nano Lett.* **2020**, *20*, 4748–4753.
[14] Schierning, G.; Theissmann, R.; Stein, N.; Petermann, N.; Becker, A.; Engenhorst, M.; Kessler, V.; Geller, M.; Beckel, A.; Wiggers, H. et al. Role of oxygen on microstructure and thermoelectric properties of silicon nanocomposites. *J. Appl. Phys.* **2011**, *110*, 113515.
[15] Kessler, V.; Dehnen, M.; Chavez, R.; Engenhorst, M.; Stoetzel, J.; Petermann, N.; Hesse, K.; Huelser, T.; Spree, M.; Stiewe, C. et al. Fabrication of high-temperature-stable thermoelectric generator modules based on nanocrystalline silicon. *J. Electron. Mater.* **2014**, *43*, 1389–1396.
[16] Claudio, T.; Schierning, G.; Theissmann, R.; Wiggers, H.; Schober, H.; Koza, M. M.; Hermann, R. P. Effects of impurities on the lattice dynamics of nanocrystalline silicon for thermoelectric application. *J. Mater. Sci.* **2013**, *48*, 2836–2845.
[17] Claudio, T.; Stein, N.; Stroppa, D. G.; Klobes, B.; Koza, M. M.; Kudejova, P.; Petermann, N.; Wiggers, H.; Schierning, G.; Hermann, R. P. Nanocrystalline silicon: Lattice dynamics and enhanced thermoelectric properties. *Phys. Chem. Chem. Phys.* **2014**, *16*, 25701–25709.
[18] Petermann, N.; Stötzel, J.; Stein, N.; Kessler, V.; Wiggers, H.; Theissmann, R.; Schierning, G.; Schmechel, R. Thermoelectrics from silicon nanoparticles: The influence of native oxide. *Eur. Phys. J. B* **2015**, *88*, 163.
[19] Tang, J. Y.; Wang, H. T.; Lee, D. H.; Fardy, M.; Huo, Z. Y.; Russell, T. P.; Yang, P. D. Holey silicon as an efficient thermoelectric material. *Nano Lett.* **2010**, *10*, 4279–4283.
[20] de Boor, J.; Kim, D. S.; Ao, X.; Becker, M.; Hinsche, N. F.; Mertig, I.; Zahn, P.; Schmidt, V. Thermoelectric properties of porous silicon. *Appl. Phys. A* **2012**, *107*, 789–794.
[21] Boukai, A. I.; Bunimovich, Y.; Tahir-Kheli, J.; Yu, J. K.; Goddard III, W. A.; Heath, J. R. Silicon nanowires as efficient thermoelectric materials. *Nature* **2008**, *451*, 168–171.
[22] Hochbaum, A. I.; Chen, R. K.; Delgado, R. D.; Liang, W. J.; Garnett, E. C.; Najarian, M.; Majumdar, A.; Yang, P. D. Enhanced thermoelectric performance of rough silicon nanowires. *Nature* **2008**, *451*, 163–167.
[23] Maire, J.; Anufriev, R.; Hori, T.; Shiomi, J.; Volz, S.; Nomura, M. Thermal conductivity reduction in silicon fishbone nanowires. *Sci. Rep.* **2018**, *8*, 4452.
[24] Lee, S.; Kim, K.; Kang, D. H.; Meyyappan, M.; Baek, C. K. Vertical silicon nanowire thermoelectric modules with enhanced thermoelectric properties. *Nano Lett.* **2019**, *19*, 747–755.
[25] Bracht, H.; Eon, S.; Frieling, R.; Plech, A.; Issenmann, D.; Wolf, D.; Hansen, J. L.; Larsen, A. N.; Ager III, J. W.; Haller, E. E. Thermal conductivity of isotopically controlled silicon nanostructures. *New J. Phys.* **2014**, *16*, 015021.
[26] Hofmann, T.; Wallacher, D.; Toft-Petersen, R.; Ryll, B.; Reehuis, M.; Habicht, K. Phonons in mesoporous silicon: The influence of nanostructuring on the dispersion in the Debye regime. *Microporous Mesoporous Mater.* **2017**, *243*, 263–270.
[27] Hofmann, T.; Kojda, D.; Haseeb, H.; Wallacher, D.; Sobolev, O.; Habicht, K. Phonons in highly-crystalline mesoporous silicon: The absence of phonon-softening upon structuring silicon on sub-10 nanometer length scales. *Microporous Mesoporous Mater.* **2021**, *312*, 110814.
[28] Zong, L. Q.; Zhu, B.; Lu, Z. D.; Tan, Y. L.; Jin, Y.; Liu, N.; Hu, Y.; Gu, S.; Zhu, J.; Cui, Y. Nanopurification of silicon from 84% to 99. 999% purity with a simple and scalable process. *Proc. Natl. Acad. Sci.* **2015**, *112*, 13473–13477.
[29] Djurdjevic, M. B.; Manasijević, S.; Odanović, Z.; Dolić, N. Calculation of liquidus temperature for aluminum and magnesium alloys applying method of equivalency. *Adv. Mater. Sci. Eng.* **2013**, *2013*, 170527.
[30] van Gestel, D.; Gordon, I.; Poortmans, J. Aluminum-induced crystallization for thin-film polycrystalline silicon solar cells: Achievements and perspective. *Sol. Energy Mater. Sol. Cells* **2013**, *119*, 261–270.
[31] Nisar, A.; Zhang, C.; Boesl, B.; Agarwal, A. Unconventional materials processing using spark Plasma sintering. *Ceramics* **2021**, *4*, 20–39.
[32] Warmuzek, M. *Aluminum-silicon Casting Alloys: An Atlas of Microfractographs*; ASM International: Materials Park, 2004.
[33] Jia, Y. D.; Cao, F. Y.; Ma, P.; Scudino, S.; Eckert, J.; Sun, J. F.; Wang, G. Microstructure and thermal conductivity of hypereutectic Al-high Si produced by casting and spray deposition. *J. Mater. Res.* **2016**, *31*, 2948–2955.
[34] Kirkpatrick, S. Percolation and conduction. *Rev. Mod. Phys.* **1973**, *45*, 574–588.
[35] Shante, V. K. S.; Kirkpatrick, S. An introduction to percolation theory. *Adv. Phys.* **1971**, *20*, 325–357.
[36] Nan, C. W. Physics of inhomogeneous inorganic materials. *Prog. Mater. Sci.* **1993**, *37*, 1–116.
[37] Gostkowska-Lekner, N.; Wallacher, D.; Grimm, N.; Habicht, K.; Hofmann, T. A novel electrochemical anodization cell for the synthesis of mesoporous silicon. *Rev. Sci. Instrum.* **2020**, *91*, 105113.
[38] Guillon, O.; Gonzalez-Julian, J.; Dargatz, B.; Kessel, T.; Schierning, G.; Räthel, J.; Herrmann, M. Field-assisted sintering technology/spark plasma sintering: Mechanisms, materials, and technology developments. *Adv. Eng. Mater.* **2014**, *16*, 830–849.
[39] Subramaniam, A. B.; Abkarian, M.; Mahadevan, L.; Stone, H. A. Non-spherical bubbles. *Nature* **2005**, *438*, 930.
[40] Jones, S. W. Diffusion in silicon [Online]. http://www-eng.lbl.gov/~shuman/NEXT/MATERIALS&COMPONENTS/Xe_damage/Diffusionin%20siliconpdf.pdf (accessed Apr 25, 2008).
[41] Montes, J. M.; Cuevas, F. G.; Cintas, J. Porosity effect on the electrical conductivity of sintered powder compacts. *Appl. Phys. A* **2008**, *92*, 375–380.
[42] Nan, C. W.; Birringer, R.; Clarke, D. R.; Gleiter, H. Effective thermal conductivity of particulate composites with interfacial thermal resistance. *J. Appl. Phys.* **1997**, *81*, 6692–6699.
[43] Chakraborty, D.; Foster, S.; Neophytou, N. Monte Carlo phonon transport simulations in hierarchically disordered silicon nanostructures. *Phys. Rev. B* **2018**, *98*, 115435.
[44] de Sousa Oliveira, L. R.; Vargiamidis, V.; Neophytou, N. Modeling thermoelectric performance in nanoporous nanocrystalline silicon. *IEEE Trans. Nanotechnol.* **2019**, *18*, 896–903.
[45] Callaway, J. Model for lattice thermal conductivity at low temperatures. *Phys. Rev.* **1959**, *113*, 1046–1051.
[46] Jeong, C.; Datta, S.; Lundstrom, M. Thermal conductivity of bulk and thin-film silicon: A Landauer approach. *J. Appl. Phys.* **2012**, *111*, 093708.
[47] Pietrak, K.; Wiśniewski, T. S. A review of models for effective thermal conductivity of composite materials. *J. Power Technol.* **2015**, *95*, 14–24.
[48] Aroutiounian, V. M.; Ghulinyan, M. Z. Electrical conductivity mechanisms in porous silicon. *Phys. Stat. Sol. (A)* **2003**, *197*, 462–466.
[49] Hori, T.; Shiomi, J.; Dames, C. Effective phonon mean free path in polycrystalline nanostructures. *Appl. Phys. Lett.* **2015**, *106*, 171901.
[50] Limbrunner, J. F.; Vogel, R. M.; Brown, L. C. Estimation of harmonic mean of a lognormal variable. *J. Hydrol. Eng.* **2000**, *5*, 59–66.
[51] de Boor, J.; Kim, D. S.; Ao, X.; Hagen, D.; Cojocaru, A.; Föll, H.; Schmidt, V. Temperature and structure size dependence of the thermal conductivity of porous silicon. *Europhys. Lett.* **2011**, *96*, 16001.
[52] Minnich, A.; Chen, G. Modified effective medium formulation for the thermal conductivity of nanocomposites. *Appl. Phys. Lett.* **2007**, *91*, 073105.